Island size evolution and molecular diffusion during growth of organic thin films followed by time-resolved specular and off-specular scattering

C. Frank,[1] J. Novák,[1,2] R. Banerjee,[1] A. Gerlach,[1] F. Schreiber,[1] A. Vorobiev,[3] and S. Kowarik[4]

[1]*Institut für Angewandte Physik, Universität Tübingen, Auf der Morgenstelle 10, 72076 Tübingen, Germany*
[2]*Central European Institute of Technology, Masaryk University, Kamenice 5, CZ-62500 Brno, Czech Republic*
[3]*ESRF, 6 Rue Jules Horowitz, Boîte Postale 220, 38043 Grenoble Cedex 9, France*
[4]*Institut für Physik, Humboldt Universität Berlin, Newtonstraße 15, 12489 Berlin, Germany*

We report on a combined off-specular and specular x-ray scattering growth study of ultrathin films of the prototypical organic semiconductor diindenoperylene (DIP, $C_{32}H_{16}$). We investigate the evolution of the in-plane correlation length and the growth kinetics of the films including their dependence on the substrate temperature and the growth rate. We observe a temperature-dependent collective rearrangement of DIP molecules from a transient surface induced to the thin-film phase, which can be rationalized by incorporating a thickness-dependent out-of-plane lattice parameter. We further observe that the nucleation behavior of DIP changes from the first to the second monolayer, which we relate to a difference in the diffusion length of the molecules.

I. INTRODUCTION

Substantial experimental as well as theoretical efforts have been made to establish a molecular level understanding of the physics underlying the growth of organic thin films [1–5]. Yet, connecting microscopic and macroscopic processes such as molecular diffusion and island size evolution remains a serious challenge. This is particularly true for rod-shaped organic semiconductor molecules because of their additional degrees of freedom, i.e., tilting (for nonspherical compounds) and bending (for flexible compounds). In this context, diindenoperylene (DIP, $C_{32}H_{16}$) is known to exhibit the complexities of the growth process rather typical for molecular systems with shape anisotropy [6–9]. These can include, e.g., rapid roughening, thickness-dependent lattice parameters, and the competition of different structural phases. Since some of these effects may be transient, a key to their understanding is real-time investigations [10–12]. An important aspect is the evolution of the lateral island size l (see Ref. [13]), which not only can be used to optimize the thin-film growth, but also provides information on the surface diffusion.

In this paper, we investigate the growth of DIP with film thicknesses of only a few monolayers (ML) on native silicon oxide at different deposition rates and substrate temperatures. Simultaneous recording of the specular [14–16] and the off-specular (diffuse) [14] intensities (see Fig. 1), which is performed *in situ* and in real time in this study, allows one to gain insight into the growth mechanisms and evolution of islands of such anisotropic organic molecules. Notably, the specular signal was measured at a fixed incidence angle, which was chosen to coincide with the so-called anti-Bragg point [16,17], i.e., at half of the reciprocal lattice vector belonging to the (001) reflection of the DIP σ phase [7]. Among the prevalent off-specular scattering techniques, grazing incidence small angle x-ray scattering (GISAXS) [18,19] is the ideal tool to characterize the growth process *in situ* in a noninvasive way. While the intensity at the anti-Bragg point contains time-resolved information on the out-of-plane film structure [20], the off-specular scattering in the vicinity of the critical angle α_c (Yoneda wings) [21,22] can be exploited to

observe changes of the in-plane film morphology. This can be realized by the use of high brilliance synchrotron radiation in combination with a fast area detector with high dynamic range.

In particular, the oscillations of the specular intensity (which were extracted from the GISAXS images taken during film growth by choosing an appropriate region around the specular reflection at the anti-Bragg point) are analyzed taking into account a thickness-dependent out-of-plane lattice parameter in order to determine the different layer coverages. The evolution of the diffuse signal (extracted by choosing a suitable region in the vicinity of the Yoneda wings) is then used to follow the film thickness dependence of the average island size. Henceforth, any reference to "specular" and "diffuse growth oscillations" would correspond to the differently oscillating intensities taken from the respective part of the GISAXS profiles, as mentioned above. GISAXS measurements are complemented by *ex situ* x-ray reflectivity (XRR) and atomic force microscopy (AFM). Using the results of these investigations, we demonstrate the influence of the activation energy barrier on the island nucleation during the initial stages of growth.

II. EXPERIMENT

DIP was purchased from the Institut für PAH Forschung (Greifenberg, Germany) with gradient sublimation purity. The films were grown on SiO_x substrates in a portable ultrahigh vacuum (UHV) chamber [23], allowing control of the substrate temperature T_{sub} (25, 50, and 100 °C) and the growth rate R_{growth} (0.1, 0.4, and 1.1 nm/min). All real-time measurements were performed at beamline ID10B of the ESRF (Grenoble, France) at a wavelength of $\lambda = 0.929$ Å and an incidence angle of $\alpha_i = 0.8°$, which corresponds to the anti-Bragg condition of the (standing up) σ phase of DIP [7,24,25]. For data acquisition a photon-counting pixel detector (MAXIPIX) was used, which provided a horizontal resolution of $\Delta q_{xy} = 2.8 \times 10^{-3}$ Å and a dynamic range of 2×10^5 counts/pixel.

In order to measure the in-plane and the out-of-plane structural evolution simultaneously, the GISAXS scattering
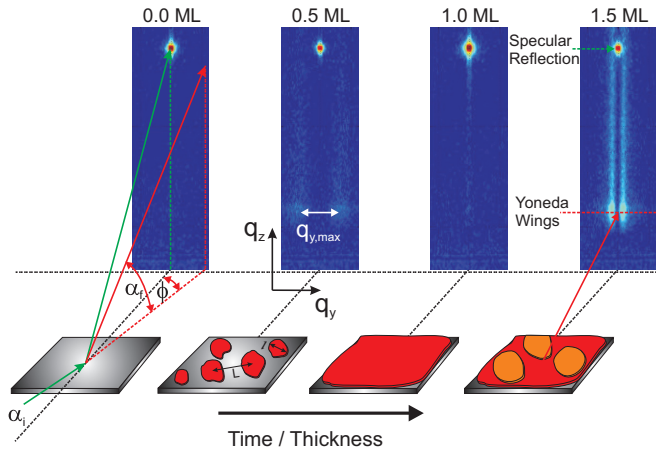
FIG. 1. (Color online) Scattering geometry, typically used in GISAXS experiments. Recording data with submonolayer time resolution allows one to follow the growth in real time. A gradual filling of successive layers leads to an oscillating intensity of the vertical streaks in the image series. The separation $q_{y,\,max}$ of these features around the Yoneda wings can be related to the average island-to-island distance L and for a known molecular coverage in the layer also to the average island diameter l.

geometry (as shown in Fig. 1) was employed. Corresponding to a wavelength of $\lambda = 0.929$ Å, the critical angle (α_c) of DIP was $0.12°$. Both the specular (i.e., $\alpha_i = \alpha_f = 0.8°$, $\phi = 0°$) and the GISAXS (i.e., $\alpha_f \approx \alpha_c$, $\phi \neq 0°$) signal are analyzed as a function of time. This allows a self-consistent thickness calibration in units of monolayer equivalents.

III. RESULTS AND DISCUSSION

Figure 2 shows the evolution of the GISAXS intensity profiles integrated within the region $q_z = 1.03$–1.30 nm^{-1} as a function of adsorbed material and the in-plane momentum transfer q_y. The chosen range includes the Yoneda wings, thus providing information on the characteristic surface correlation length. The associated time resolution was $\simeq 15$ frames/ML, where each frame has been exposed for 20 s. The appearance of two relatively weak correlation peaks at the very beginning of the growth ($q_y \simeq 0.17$ nm^{-1}) indicates the existence of a well-defined correlation length, which corresponds to the average island-to-island distance L. Below one ML coverage, we observe a significant change in the intensity as well as in the position of these correlation peaks. The shift towards smaller values of q_y ($\simeq 0.05$ nm^{-1}) implies that the island-to-island distance, measured from the island's center of mass (see Fig. 1), increases as the first layer is being filled. At a coverage of 1 ML both peaks disappear, which points to the absence of any noticeable long-range surface modulations for the smooth, completely filled first ML. The off-specular intensity oscillates between a maximum at half-filled layers to a minimum at the completion of subsequent layers. During the growth of the second ML the peaks appear at still smaller values of q_y ($\simeq 0.03$ nm^{-1}). Above ~ 3 ML we observe two intense streaks, which do not change position with respect to q_y, accounting for an average correlation length scale which is representative
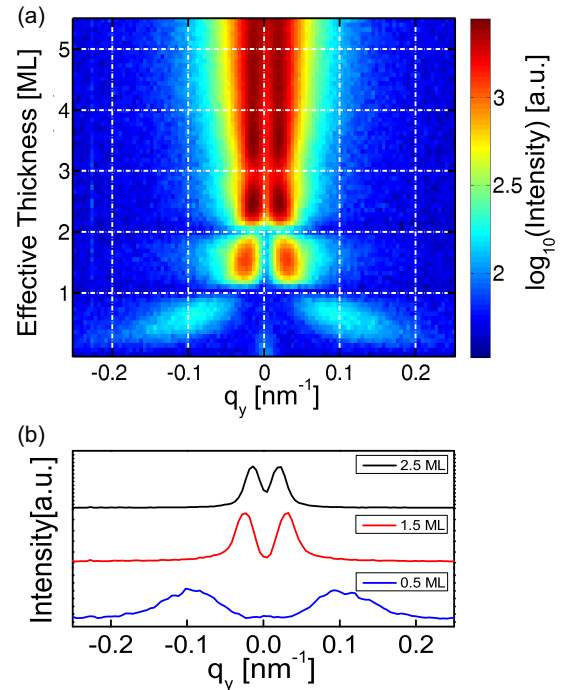

FIG. 2. (Color online) (a) Scattering intensity at the critical angle (Yoneda wings) as a function of adsorbed material for DIP grown at $T_{sub} = 25$ °C and $R_{growth} = 0.1$ nm/min. Detector images from which the horizontal GISAXS sections have been extracted, were integrated for 20 s per frame leading to a resolution of $\simeq 15$ frames/ML. (b) Horizontal line sections [extracted from the GISAXS images in (a)] at coverages of $\theta = 0.5$, 1.5, and 2.5 ML. It is clearly observed that the separation between the two correlation peaks decreases for higher film coverages. As the growth progresses, more material is adsorbed on the surface and the correlation peaks become more intense.

of the finite average distance of the DIP mounds. This is a clear signature of a transition from the layer-by-layer (LBL) to the three-dimensional (3D) growth, i.e., formation of molecular islands, which is analogous to the classical Stranski-Krastanov growth mode. Similar observations were made for other growth conditions of the film (e.g., different temperature and growth rate), indicating that in general for DIP the first ML is always completely filled before the second or subsequent ML grows on top of it. Generally, the critical thickness, at which a transition from the LBL to the 3D growth occurs, depends nontrivially on R_{growth} and T_{sub} and requires separate systematic investigations to gain further detailed knowledge.

A. Analysis of the out-of-plane structure

To probe the dependence of the out-of-plane structure on the growth conditions, we have analyzed the thickness-dependent intensity at the anti-Bragg point (corresponding to $q_z = 1.87$ nm^{-1}) using a combination of a growth model first proposed by Trofimov *et al.* [26] and kinematic scattering theory [8,16,20] [see Figs. 3(a)–3(c)].
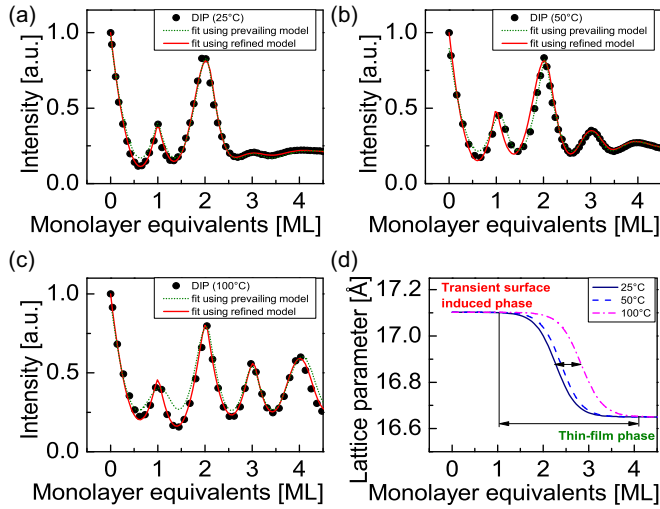
FIG. 3. (Color online) (a)–(c) Specular oscillations at the anti-Bragg point (scatter plots) for DIP grown at $T_{sub} = 25$, 50, and 100 °C and $R_{growth} = 0.4$ nm/min. The data were fitted using the prevailing model (PM) but show a considerable deviation during the filling of the second ML. However, the fit improved remarkably once the refined model (RM) has been applied. (d) Using the refined model the thickness dependence of the out-of-plane lattice parameter was determined for three different temperatures, showing an orientational transition from the transient surface induced to the thin-film phase. Importantly, the transition is delayed for higher substrate temperatures.

According to this prevailing model (PM) the total scattering intensity is given by

$$I(t) = \left| A_{sub}(q_z)e^{i\phi} + c \sum_n \theta_n(t)e^{-inq_z d} \right|^2, \tag{1}$$

where A_{sub} is the scattering amplitude, ϕ the phase shift, c the molecular layer form factor, θ_n the coverage of layer n, q_z the out-of-plane momentum transfer, and d the out-of-plane lattice parameter. We find that this model deviates considerably from the observed intensities during the growth of the second ML for all DIP samples grown at high substrate temperatures (see Fig. 3). Organic molecules with shape anisotropy may exhibit a change of their tilt angle [4]—an effect which is not considered in Eq. (1). In particular, for the molecular system DIP/SiO$_x$ previous studies reveal kinetically determined orientational and structural transitions of the molecular layer, which (depending on the substrate material) take place in the first few-monolayer regime [7] and can be related to a thickness-dependent interlayer mass transport [9,27]. This collective change of the molecular tilt angle potentially involves all layers simultaneously. Therefore, we introduce thickness-dependent parameters (c', Φ, d'), where Φ is the phase of the now complex layer form factor $c'e^{i\Phi}$. To determine at which stage and how gradually the collective change occurs, the variation of the lattice parameter (as a function of thickness) is obtained from analyzing the XRR profiles of the films (see Fig. 4). The XRR data were fitted using the Parratt formalism [28,29]. The electron density profiles and the respective out-of-plane lattice parameters obtained from
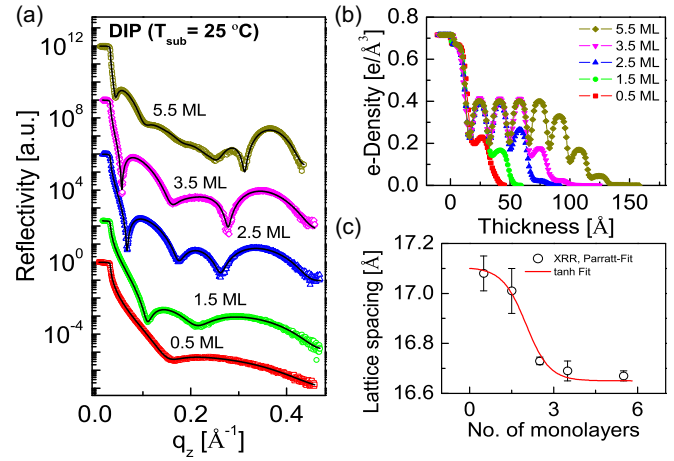

FIG. 4. (Color online) (a) *Ex situ* postgrowth XRR scans (open symbols) of DIP grown at a substrate temperature of $T_{sub} = 25$ °C and a growth rate of $R_{growth} = 0.1$ nm/min. The film thickness was varied between 0.5 and 5.5 ML. Solid lines show fits based on the Parratt formalism. (b) Corresponding electron densities plotted against the nominal film thickness. (c) Out-of-plane lattice parameters obtained from the XRR data shown in panel (a) (open circles) and the respective tanh-functional fit (solid line).

the fits are shown in Figs. 4(b) and 4(c), respectively. Finding that the change in the lattice parameter can be well described using a tanh-functional dependence [Fig. 4(c)], we introduce an empirical variation of the three parameters c', Φ, and d' (which, for the sake of convenience, are combined in a vector $\boldsymbol{P}$), according to

$$\boldsymbol{P}_{\gamma, t_0} = \boldsymbol{P}_\infty + \frac{\Delta \boldsymbol{P}}{2}(\tanh[\gamma(t - t_0)] - 1). \tag{2}$$

From our data we are able to extract the asymptotic value $\boldsymbol{P}_\infty \equiv \boldsymbol{P}(t \to \infty)$, the variation $\Delta \boldsymbol{P} \equiv \boldsymbol{P}(t = t_0) - \boldsymbol{P}(t \to \infty)$, and the steepness parameter γ. Fitting the anti-Bragg growth oscillations with this function results in a remarkable agreement [see Figs. 3(a)–3(c)].

Importantly, the change of the out-of-plane lattice depends on the growth temperature. For example, we observe that while the fit for 100 °C reproduces the experimental data very well, using the same functional dependence of the lattice parameter and complex layer form factor for a different temperature (say 25 °C) leads to a markedly different intensity profile. Figure 3(d) shows the thickness-dependent evolution of the out-of-plane lattice parameter of the thin films at the same R_{growth} (0.4 nm/min) for three different T_{sub}. We find that the transition from the transient to the stable thin-film phase, which results in a lattice spacing decrease of ~ 0.5 Å, occurs between 2 and 4 ML [see Fig. 3(d)]. Interestingly, this change in the molecular tilt angle occurs simultaneously with the transition from the LBL to the 3D growth. Additionally, we observe a delay in this collective molecular tilting (to the stable thin-film orientation) for the films grown at a higher substrate temperature. We attribute this delay to the fact that the strength of the long-range in-plane cohesive interaction depends on the dimensions of the islands. Within the model description it is quite reasonable to assume that the close packing of molecules within an island confines
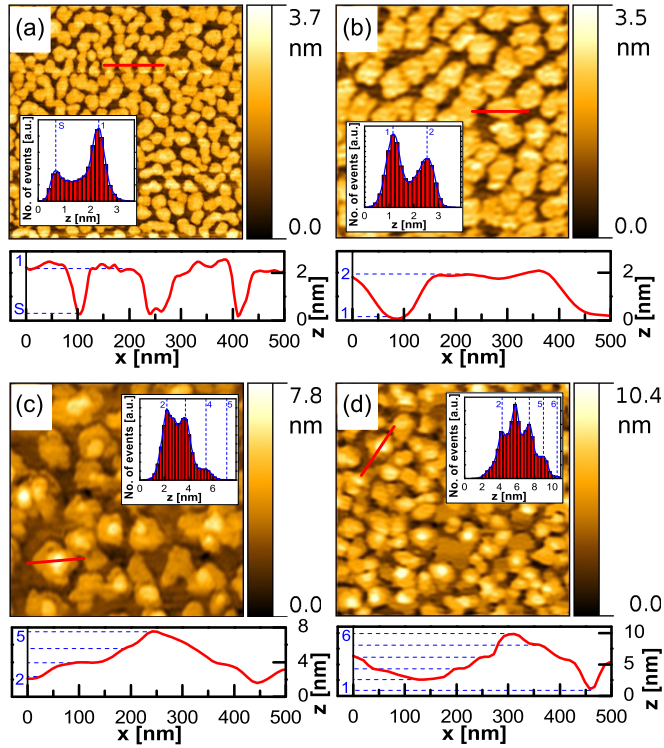
FIG. 5. (Color online) AFM images of DIP grown at $T_{\text{sub}} = 25\ ^\circ$C and $R_{\text{growth}} = 0.1$ nm/min taken with a JPK Nanowizard II. Respective height distributions are shown in the insets. Line profiles (indicated by red lines) are shown below the respective images. The images are shown for coverages of ~ 0.5, ~ 1.5, ~ 3.5, and ~ 5.5 ML [(a)–(d)] and cover an area of $2 \times 2\ \mu$m^2.
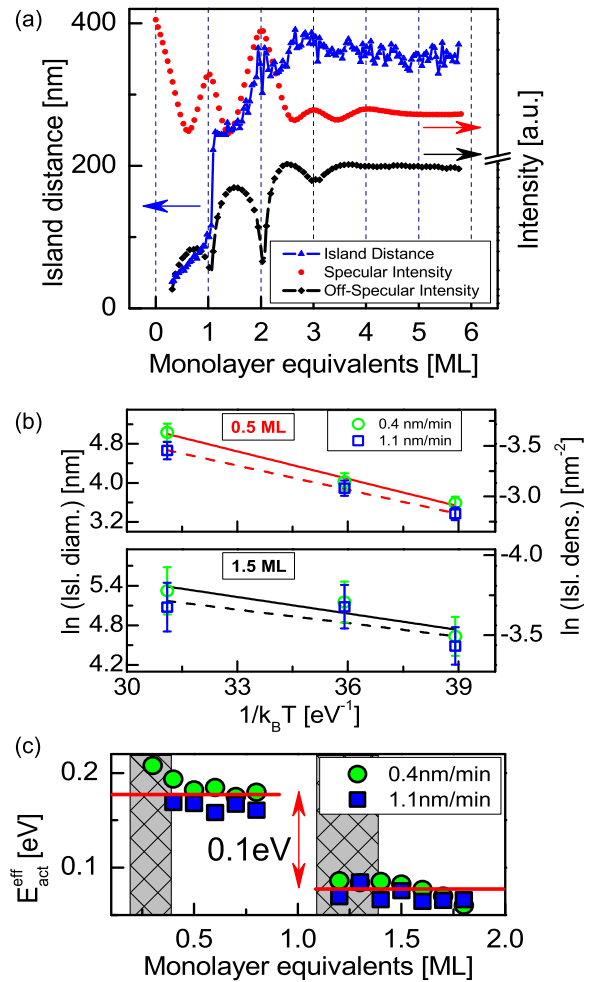

FIG. 6. (Color online) (a) Average island distance (left axis), and specular and diffuse intensity (right axis) obtained by fitting the GISAXS data for DIP grown at $T_{\text{sub}} = 25\ ^\circ$C. (b) Arrhenius plot for two different growth rates and two different thicknesses. The solid lines correspond to linear fits of $R_{\text{growth}} = 0.4$ nm/min and the dashed lines to $R_{\text{growth}} = 1.1$ nm/min, respectively. (c) Effective activation energy of nucleation $E_{\text{act}}^{\text{eff}}$ calculated for different coverages, which are almost constant throughout the layer filling. Note that $E_{\text{act}}^{\text{eff}}$ was derived using Eq. (3), which is valid only for small coverages (shown here as shaded areas).

their respective molecular movements (including tilting). In particular, the more molecules are involved (i.e., the larger the island size), the more difficult it is to collectively cause the molecules to flip within that island. Consequently, we expect that the critical point, where the collective tilting occurs, depends on the parameters describing the shape of the islands, i.e., for disk-shaped islands (as observed in this study) the island diameter and height. Because increasing T_{sub} leads to larger islands (as discussed later), the tilt is delayed.

B. Analysis of the in-plane morphology

AFM was performed post growth to complement our scattering measurements on the same set of samples with various thicknesses (0.5–5.5 ML) and coverages (see Fig. 5).

At ~ 0.5 ML two-dimensional (2D) compact islands, which already start to coalesce, form on the substrate. At ~ 1.5 ML the substrate is completely covered by the first layer [Fig. 5(b), inset], which serves as a template for the nucleation of the second layer. We also observe that islands nucleating on top of the first layer are significantly larger than those on SiO$_x$. For higher coverages [Figs. 5(c) and 5(d)] we observe mound formation with the second layer providing the base for the mounds. This indicates a very pronounced LBL growth during the early stages, followed by a transition to islandlike growth as was also observed in the GISAXS data [Fig. 2(a)].

For the quantitative analysis of the real-time GISAXS, we deduce the mean island-to-island distance $L = 2\pi/|q_{y,\max}|$ from the position of the two correlation peaks using Lorentzian fits of the Yoneda wing at an exit angle $\alpha_f \simeq \alpha_c$ [Fig. 6(a)]. As expected for the initial LBL growth, the specular intensity oscillates up to ~ 3 ML. The subsequent 3D growth results in a rapid damping of the oscillations. Importantly, the diffuse scattering intensity also exhibits pronounced oscillations in the LBL regime with maxima at half-filled layers and minima for closed layers. This anticorrelation of specular and diffuse intensities is related to the periodically changing surface roughness, i.e., for half-filled layers the roughness takes on a maximum. A sudden change of the island distance after filling the first layer accounts for the nucleation of new widely spaced islands in the second ML. Additionally, we find that islands

nucleating on top of the first layer are significantly larger than on top of the substrate, as also confirmed by AFM.

To derive the average island diameter l we approximate DIP islands as 2D disks and combine the layer coverage θ_n (obtained by fitting the anti-Bragg oscillations) with the island distance L given by $l = 2L\sqrt{\theta_n/\pi}$. Figure 6(b) shows that the island diameter extracted at coverages of 0.5 and 1.5 ML consistently follows the same trend within the investigated temperature/growth rate regime. For example, at $R_{growth} = 0.4$ nm/min and a coverage of 0.5 ML (1.5 ML) we find that the island size increases from $l = 36$ nm (103 nm) to $l = 153$ nm (205 nm), when increasing the substrate temperature from 25 °C to 100 °C. Increasing the growth rate to $R_{growth} = 1.1$ nm/min has less impact on the island size and leads to only marginally smaller islands. Importantly, we observe that the nucleation of larger islands in the second layer is a general feature of DIP growth under different conditions. We relate this behavior to a significant difference between the molecule-substrate interaction (dominant during the initial stage of growth) versus the molecule-molecule interaction (dominant during the later stages of growth), which leads to a difference in the corresponding diffusion length scales.

C. Estimation of effective activation energies

The relevant growth kinetics within such systems may be obtained by comparing the effective activation energy of nucleation E_{act}^{eff} between the first and second layer. In this context, E_{act}^{eff} is derived from the Arrhenius plot of the island diameter (or alternatively island density) versus temperature [Fig. 6(b)]. The *in situ* data has been analyzed over a broad coverage regime using this approach. The different slopes in the two Arrhenius plots indicate a difference between the activation energies, and therefore also between the diffusion barriers in the first and the second layer. In dynamical 2D-nucleation theory considering small layer coverage ($\theta_n \ll 1$), the kinetics of the island growth, i.e., the time dependence of the island size and density, is related to the flux of the incoming molecules F, the surface diffusion coefficient D, the thermal energy $k_B T$, and the critical nucleus size $i^\star$ [30–32]. For the first two ML we relate l to E_{act}^{eff} via

$$l \propto \theta_n^{-(i^\star+1)/2} \left(\frac{D_0}{F} \right)^{i^\star/2(i^\star+2)} e^{-E_{act}^{eff}/k_B T}, \qquad (3)$$

where D_0 is the diffusion preexponential factor. The activation energy is proportional to the diffusion barrier E_D and binding energy $E_{i^\star}$ of clusters consisting of $i^\star$ molecules and, in conventional theory, [4,13,33] given by $E_{act}^{eff} = (i^\star E_D + E_{i^\star})/2(i^\star + 2)$. Note that a precise determination of $E_{i^\star}$ turns out to be very difficult. Even for comparatively simple inorganic systems, such as Pt grown on Pt(110), the experimentally obtained binding energy of a Pt dimer differs from those estimated by density functional calculations [33–35] by 66%. For molecular systems with shape anisotropy orientational degrees of freedom arise, which implies that even $E_{i^\star}$ (and actually, in principle, also E_D) are not unique numbers, since they depend on the *relative orientation* of the molecules. These issues call for an extension of the theoretical description on a fundamental level, as e.g., also seen in previous results on the growth exponents [6,7]. Therefore, we restrict ourselves to

TABLE I. Effective activation energy of nucleation E_{act}^{eff} for the first and second layers obtained by taking the layer-specific average of the data shown in Fig. 6(c). The error bars for E_{act}^{eff} correspond to the standard deviation of the different data sets.

	R_{growth}	E_{act}^{eff}	ΔE_{act}^{eff}
Layer 1 (DIP on SiO$_x$)	0.4 nm/min	0.19 ± 0.01 eV	0.11 eV
Layer 2 (DIP on DIP)		0.08 ± 0.01 eV	
Layer 1 (DIP on SiO$_x$)	1.1 nm/min	0.16 ± 0.04 eV	0.09 eV
Layer 2 (DIP on DIP)		0.07 ± 0.01 eV	

the determination of the effective activation energy for island nucleation. The effective activation energies thus determined for different coverages are shown in Fig. 6(c) and summarized in Table I. For both growth rates, we observe a consistent difference of $\Delta E_{act}^{eff} \approx 0.1$ eV between the first and second molecular layer. This implies an increase of the diffusion length of DIP in the second layer, which leads to a longer migration time of monomers and thus explains the observed formation of larger islands.

IV. CONCLUSION

We have used real-time x-ray specular and diffuse scattering to study *in situ* the dynamics of DIP thin-film growth on silicon oxide, namely, the thickness-dependent evolution of lattice parameters, island size evolution, and surface diffusion processes. We have introduced an improvement on the existing model for simulations of anti-Bragg growth oscillations by including the effect of the change in the molecular tilt angle during growth. We suggest that the observed molecular tilting from the transient surface induced towards the stable thin-film phase orientation is related to a change in the interlayer transport leading to the transition to 3D growth. Furthermore, we have used real-time GISAXS to study the island size evolution during deposition of DIP. The smaller diffusion activation energy on top of the first molecular layer results in a larger diffusion length and hence the formation of bigger islands than on the silicon oxide substrate, where the activation energy is ∼0.1 eV larger. For DIP on SiO$_x$, this seems to be a rather general phenomenon at various growth rates and substrate temperatures.

We have provided a systematic x-ray scattering study to investigate in real time the growth behavior of rodlike organic semiconducting molecules. The evolution of island sizes and differences of the molecular diffusion in the very first layers are important questions that need to be addressed—also for more complex systems such as binary mixtures [36–38]. Our results provide key insights into this rich field, which could be used for the development of new theoretical models of growth that go beyond the existing formalism by including shape anisotropy.

[1] W. Brütting and C. Adachi, *Physics of Organic Semiconductors*, 2nd ed. (Wiley-VCH, Weinheim, 2012).

[2] M. Fendrich and J. Krug, Phys. Rev. B **76**, 121302 (2007).

[3] A. Pimpinelli and J. Villain, *Physics of Crystal Growth* (Cambridge University Press, Cambridge, 1998).

[4] G. Hlawacek, P. Puschnig, P. Frank, A. Winkler, C. Ambrosch-Draxl, and C. Teichert, Science **321**, 108 (2008).

[5] J. E. Goose, E. L. First, and P. Clancy, Phys. Rev. B **81**, 205310 (2010).

[6] A. C. Dürr, F. Schreiber, K. A. Ritley, V. Kruppa, J. Krug, H. Dosch, and B. Struth, Phys. Rev. Lett. **90**, 016104 (2003).

[7] S. Kowarik, A. Gerlach, S. Sellner, F. Schreiber, L. Cavalcanti, and O. Konovalov, Phys. Rev. Lett. **96**, 125504 (2006).

[8] A. R. Woll, T. V. Desai, and J. R. Engstrom, Phys. Rev. B **84**, 075479 (2011).

[9] X. Zhang, E. Barrena, D. Goswami, D. G. de Oteyza, C. Weis, and H. Dosch, Phys. Rev. Lett. **103**, 136101 (2009).

[10] S. Kowarik, A. Gerlach, and F. Schreiber, J. Phys.: Condens. Matter **20**, 184005 (2008).

[11] T. V. Desai, A. R. Woll, F. Schreiber, and J. R. Engstrom, J. Phys. Chem. C **114**, 20120 (2010).

[12] S. Hong, A. Amassian, A. R. Woll, S. Bhargava, J. D. Ferguson, G. G. Malliaras, J. D. Brock, and J. R. Engstrom, Appl. Phys. Lett. **92**, 253304 (2008).

[13] R. Ruiz, B. Nickel, N. Koch, L. C. Feldman, R. F. Haglund, A. Kahn, F. Family, and G. Scoles, Phys. Rev. Lett. **91**, 136102 (2003).

[14] J. D. Ferguson, G. Arikan, D. S. Dale, A. R. Woll, and J. D. Brock, Phys. Rev. Lett. **103**, 256103 (2009).

[15] S. Kowarik, A. Gerlach, A. Hinderhofer, S. Milita, F. Borgatti, F. Zontone, T. Suzuki, F. Biscarini, and F. Schreiber, Phys. Status Solidi RRL **2**, 120 (2008).

[16] S. Kowarik, A. Gerlach, M. W. A. Skoda, S. Sellner, and F. Schreiber, Eur. Phys. J.: Spec. Top. **167**, 11 (2009).

[17] A. Amassian, T. V. Desai, S. Kowarik, S. Hong, A. R. Woll, G. G. Malliaras, F. Schreiber, and J. R. Engstrom, J. Chem. Phys. **130**, 124701 (2009).

[18] P. Müller-Buschbaum, *Applications of Synchrotron Light to Scattering and Diffraction in Materials and Life Sciences*, edited by M. Gomez, A. Nogales, M. C. Garcia-Gutierrez, and T. Ezquerra, Lecture Notes in Physics Vol. 776 (Springer, Berlin, Heidelberg, 2009), pp. 61–89.

[19] R. Lazzari, F. Leroy, and G. Renaud, Phys. Rev. B **76**, 125411 (2007).

[20] B. Krause, F. Schreiber, H. Dosch, A. Pimpinelli, and O. H. Seeck, Europhys. Lett. **65**, 372 (2004).

[21] S. K. Sinha, E. B. Sirota, S. Garoff, and H. B. Stanley, Phys. Rev. B **38**, 2297 (1988).

[22] U. Pietsch, V. Holý, and T. Baumbach, *High-Resolution X-Ray Scattering: From Thin Films to Lateral Nanostructures* (Springer-Verlag, New York, 2004).

[23] K. A. Ritley, B. Krause, F. Schreiber, and H. Dosch, Rev. Sci. Instrum. **72**, 1453 (2001).

[24] A. Dürr, B. Nickel, V. Sharma, U. Täffner, and H. Dosch, Thin Solid Films **503**, 127 (2006).

[25] Y. L. Huang, W. Chen, H. Huang, D. C. Qi, S. Chen, X. Y. Gao, J. Pflaum, and A. T. S. Wee, J. Phys. Chem. C **113**, 9251 (2009).

[26] V. I. Trofimov and V. G. Mokerov, Thin Solid Films **428**, 66 (2003).

[27] X. N. Zhang, E. Barrena, D. G. de Oteyza, and H. Dosch, Surf. Sci. **601**, 2420 (2007).

[28] L. G. Parratt, Phys. Rev. **95**, 359 (1954).

[29] J. Daillant and A. Gibaud, *X-Ray and Neutron Reflectivity* (Springer, Berlin, Heidelberg, 2009).

[30] J. Krug, Eur. Phys. J. B **18**, 713 (2000).

[31] J. Krug, P. Politi, and T. Michely, Phys. Rev. B **61**, 14037 (2000).

[32] J. A. Venables, Philos. Mag. **27**, 697 (1973).

[33] T. Michely and J. Krug, *Islands, Mounds, and Atoms. Patterns and Processes in Crystal Growth Far from Equilibrium* (Springer, Berlin, 2004).

[34] T. R. Linderoth, S. Horch, L. Petersen, S. Helveg, M. Schønning, E. Lægsgaard, I. Stensgaard, and F. Besenbacher, Phys. Rev. B **61**, R2448 (2000).

[35] P. J. Feibelman, Phys. Rev. B **61**, R2452 (2000).

[36] A. Aufderheide, K. Broch, J. Novák, A. Hinderhofer, R. Nervo, A. Gerlach, R. Banerjee, and F. Schreiber, Phys. Rev. Lett. **109**, 156102 (2012).

[37] R. Banerjee, J. Novák, C. Frank, C. Lorch, A. Hinderhofer, A. Gerlach, and F. Schreiber, Phys. Rev. Lett. **110**, 185506 (2013).

[38] A. Hinderhofer and F. Schreiber, Chem. Phys. Chem. **13**, 628 (2012).